

Chapter 5

Detection and Characterisation of rotational spherical aggregate rotational dynamics

As outlined in the end of Chapter 4, one of the difficulties in characterising interactions with asymmetric objects is the coupled motion between translation and rotation. In order to characterise the optical trap a position detection system such as a lateral effect photodiode or a quadrant photo diode (see fig.??). Typically, a position detection system assumes that there exists a linear relationship between the a particle's displacement and the detected signal. However, this is not always the case as demonstrated in chapter 4; as dimer's demonstrate non-harmonic trapping beyond a certain displacement. In addition, the rotational effects of the trapped dimer become a more significant factor when characterising the trap strength. This can have unintended effects when it comes to areas of research that require a precise understanding of the hydrodynamic behaviour of particles. As such there has been a concerted effort to either eliminate rotational motion, or describe how the rotational behaviour influences the trajectory reported by the position detector.

In chapter 4 we showed that while machine learning can be used to accurately predict the translational displacements of an aggregate particle, it fails when trying to

account for the rotational behaviour of said particle. In this chapter we build upon [2] but now account for the full rotational motion. This was initially developed in tandem with the work conducted in chapter 3, with the idea being that if a crystal nucleus formed on a rotating sphere how would that nucleus influence the motion of the rotating sphere. Using static light scattering we can map the outputted signal from an optically trapped dimer to its expected orientation in real time. Thus allowing us to estimate the optical torque being applied to the dimer by the trapping beam. As demonstrated in chapter 4, the influence of a circularly polarised beam can result in gyroscopic precession for specifically sized dimers.

We start by defining the optical fibre detection system from a mathematical perspective. Before demonstrating how it can be used to instantaneously predict orientational information on a trapped particle. We then consider common factors of error in the characterisation process, such as signal error, and incorrect particle sizing. Both of which have a significant impact on the performance of the model, but by utilising Bayesian inference, and time averaging we can better refine our model.

5.1 Characterisation of asymmetric dimer dynamics via PSD analysis

As discussed in ??, one of the methods developed to work in conjunction with [7] is a simulated quadrant photo diode for as a position detection system. While it is possible to extract all of the relevant dynamical information from a simulation, confirming the same behaviour in an experimental setting can be challenging if dealing with a non-birefringent anisotropic scatterer. The QPD is composed of 4 photodiodes that measure the intensity of light incident on their surfaces. Using *ott* we can define a region in the far-field that is analogous to the surface of the QPD surface. Evaluating the electric field across this surface gives us an approximation of the QPD signal outputted in an experimental situation. This does not provide a one-to-one result however as hardware errors (i.e. internal resistance, external light sources, and vibrations) would distort the signal somewhat. We can use this as a means to examine the limitations of using

back-focal plane interferometry as a means for characterising anisotropic scatterers.

As a benchmark we start by considering a single sphere within an optical trap. A single polystyrene sphere suspended in water ($a = 1\mu m$, $n_p = 1.59$, $n_m = 1.33$) was trapped by a focused Gaussian beam ($NA = 1.25$) using circularly polarised light. For the sake of time efficiency the trajectory was sampled every 10 time steps, meaning the upper bound on the power spectra is $f_{Nyq} = f_{sample}/2 = 5000\text{ Hz}$. To optimise the frequency window we fitted the power spectra using the aliased Lorentzian (Eq. (??)).

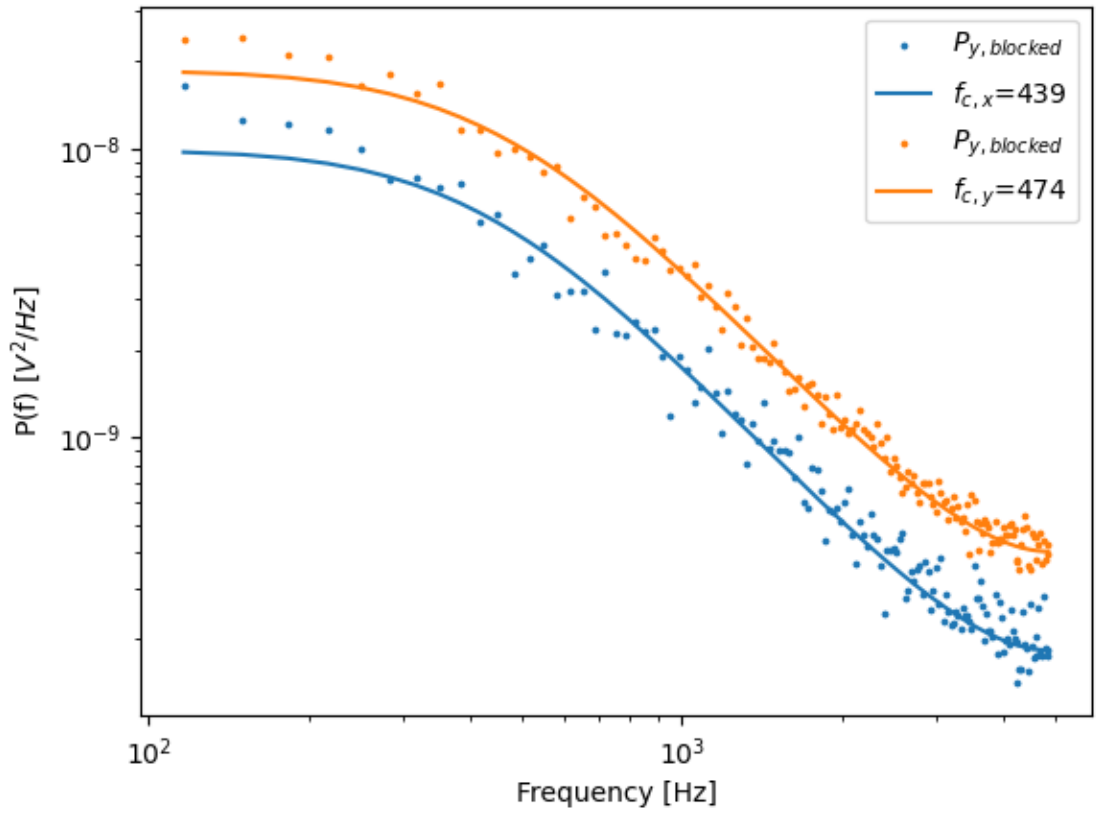


Figure 5.1: Recorded power spectra fitted to eq. ??, scattered points represents the blocked data ($n_b = 100$). Corner frequency for the Lorentzian curves are reported in the legend.

As shown in fig. 5.1, the two power spectra report different corner frequencies which would indicate that the trap is not perfectly circular. We can use both *ott* and the trajectory itself to derive an estimation of the trap geometry. Additionally, we fitted

the same Lorentzian to the sphere’s positional data, this would be a situation when the QPD signals are completely uncorrelated with one another and there is a constant ratio between the QPD signal and the sphere’s position. The corner frequencies and corresponding trap stiffness are reported below:

Table 5.1: QPD fitting for single sphere

Fitting parameter	<i>ott</i> estimates		QPD fitting		Trajectory fitting	
f_c [Hz]	447	450	439	474	523	513
$\sigma(f_c)$ [Hz]	—	—	9.30	9.65	8.67	8.61
κ [pN/ μ m]	53.05	53.40	51.96	56.09	61.94	60.7
Ellipticity	8.16 %		27.17 %		13.8 %	

Where $\sigma(f_c)$ is computed from [3], where the variance is based upon our choice of frequency boundaries ($f_{min} : f_{max} = 100 \text{ Hz} : 5000 \text{ Hz}$). And the ellipticity of the beam is given by $e = (1 - \kappa_y/\kappa_x)^{0.5}$ and is a measure of the symmetry of the beam wavefront. Its clear from these initial results that the QPD is more sensitive to changes along the y-axis than the x-axis when compared to the direct *ott* calculations. This is somewhat reflected in the trajectory results. Typically, even an industrial Gaussian beam will produce an elliptical diffraction limit spot when heavily focused; in their tutorial for optimizing the PSD analysis, Berg and Sorensen reported a ellipticity of around 15 % after a total calibration time of 80 seconds [3].

The reason for the discrepancies between all 3 methods is due to what is actually being measured. The *ott* estimates are simply looking at the differences in the trapping strength along the Cartesian axis’. If calibrated over an long enough time frame you would expect that the resulting power spectra would exactly mirror the *ott* predictions. However over a short calibration time a QPD will only sample a small trajectory that does not fully explore the trapping plane. There is a clear trade off in terms of accuracy and computation time as shorter calibration runs are computationally more efficient but prone to errors.

With this in mind, let us consider a symmetric dimer that is optically trapped by the same Gaussian beam. Not only does the dimer’s equilibrium position change but

it is subjected to rotational motion due to its unequal moments of inertia. This is reflected in the calibration results using the simulated QPD, where we see a drastically different estimation between the *ott* estimate and the QPD estimate.

Table 5.2: QPD fitting for symmetric dimer

Fitting parameter	<i>ott</i> estimate		QPD fitting		Trajectory fitting	
f_c [Hz]	445	409	431	424	274	285
$\sigma(f_c)$ [Hz]	—	—	9.22	9.16	7.82	7.91
κ [pN/ μ m]	52.82	48.54	51.13	50.26	32.45	33.75
Ellipticity	28.5 %		12.7 %		13.8 %	

Now we see that the *ott* predicts a more elliptical trap compared to the QPD model which says the trap is far more symmetrical while trapping a symmetric dimer. A potential reason that *ott* no longer expects a circular trap is because that unlike a sphere, the force displacement curve is not strictly harmonic. If we consider a dimer that is some distance from the beam axis, the sphere closest to the trap focus will experience a slightly greater force compared to the sphere further from the trap. As such its not accurate to assume that the external force $F(x) = \kappa x$ instead we must consider that it is a function of both the position and orientation simultaneously.

This coupling of the translational and orientational motion has been highlighted previously [7], but there effects have not been demonstrated in the context of an experimental situation. We can see from the difference in trajectory and QPD fittings that while our description of the trap shape is very similar (both methods give similar ellipticity values) but the magnitude of the trap strength are significantly different. This is partially explained by the fact that the QPD is not actually measuring the position of the particle but instead the intensity distribution of the total field incident on the QPD surface. In which case if the dimer is rotated slightly the QPD signal will change even if the dimers centre of diffusion remains stationary.

5.1.1 QPD for angular displacement detection

The next logical step is to consider whether or not a QPD can at all be utilised for detection of rotational motion. This has been shown for nano-particles that exhibit periodic rotational motion using by considering the difference in diagonal quadrants. The benefit of detecting rotational motion is that one can begin to build a better understanding about how angular momentum is transferred to a dimer which could be extended to more complex particles.

At just a cursory glance it would appear that there is a clear relationship between the QPD signal and the orientation of the dimer. If we look at the QPD signal produced by a dimer as it is rotated we can see that it is equally sensitive to rotations in either the X-Z or Y-Z plane but there is no change in the signal when rotated by in the X-Y plane.

However if we compare this to fig. ?? we can see that the the signal change is dwarfed by the translational motion. So while there is a clear relationship between the two trying to discern between translational and rotational contributions to the QPD signal is not a simple task. This is significant because it means that with regards to the power spectrum fittings in table 5.2 there is no way of ensuring that the measured trap strengths are accurate. The variance $\sigma(f_c)$ is only the variance based upon our fitting parameters and not on the actual dynamics of the dimer. In the case where the particle's shape is not known prior its not possible to determine whether any inaccuracies in the power spectra are due to the fit or due to the particle's motion.

The dependence of S_x and S_y and the dimer's orientation (defined by the spherical angles θ, ϕ) is therefore not clear. To that end, we utilised machine vector regression, which takes as an input the voltage from the 4 quadrants and tries to fit that to the dimer's trajectory. Fitting the QPD signal to the dimer's position shows promising results, shown in fig. X.X is a prediction of a symmetric dimer's position based on the QPD signal. With the actual displacement on the x-axis and the predicted result y-axis, and the dashed line represents the $y=x$ line - indicating an ideal prediction.

Fig X.X shows that its relatively trivial to predict a particle's position based off the QPD signal, even in axial direction which has not been done previously. It should be

noted that these displacements are relative to the trap focus and so accurate tracking of the beam movements needs to be taken. This result is partially due to the fact that displacement and signal units are linearly related by (??). Interestingly when we run the same protocol for different sized dimer's there seems to be a cut off point when the fit begins to fail. Plotting the R^2 for each fit vs its size ratio shows that beyond a size ratio of 5 the machine learning begins to fall off significantly.

This is surprising because we would expect that as the second sphere shrinks the dynamics should more closely approximate that of a single sphere. We can compare our

5.2 Monitoring Stochastic rotational motion using static light scattering

Part of the optical fibre arrangement borrows code from the optical tweezer simulations discussed in Chapter 2 and 4. Rather than repeat the simulation details we will instead only focus on the specifics of the optical fibre scattering.

5.2.1 Coordinate System

Consider a particle (either a sphere or dimer) trapped by a Gaussian beam, with its focal point being set at $[0,0,0]$. At the same time an optical fibre directs a plane wave that is incident on the trapped particle scattering light in all directions. The probe beam is assumed to be x-polarised and propagating in the $+z$ direction, this is a 90° rotation from the previous simulations (see figX.X).

5.2.2 Dimer

The dimer is defined by two spheres with refractive indices of 1.59 and suspended in water ($n_{med} = 1.33$). *MSTM* requires a target origin for setting the scattering expansion, there is no agreed upon solution for where the target origin should be relative to the sphere positions. In chapter 4 we showed that altering the target origin would drastically alter the tmatrix produced

5.2.3 Scattering and Detection

Each detector is placed some distance \mathbf{r} from the origin, detector positions are defined by angles θ & ϕ . With $\theta = \phi = 0$ being directly in front of the probe beam. The position of each detector is given by:

$$\begin{pmatrix} x_{fiber} \\ y_{fiber} \\ z_{fiber} \end{pmatrix} = \begin{pmatrix} r \cos(\phi) \sin(\theta) \\ r \sin(\phi) \sin(\theta) \\ r \cos(\theta) \end{pmatrix} \quad (5.1)$$

Where r is the distance between the detector and the target origin. In an ideal situation the surface of the detector is oriented towards the target origin perfectly. Pixels can be thought of as points lying on the surface of the detector, each point has its own position in real space. Using *mstm* we can find the components of the scattering matrix at each point and compute the intensity of the electric field via:

$$\begin{pmatrix} I_s \\ Q_s \\ U_s \\ V_s \end{pmatrix} = \begin{pmatrix} S_{11} & S_{12} & S_{13} & S_{14} \\ S_{21} & S_{22} & S_{23} & S_{24} \\ S_{31} & S_{32} & S_{33} & S_{34} \\ S_{41} & S_{42} & S_{43} & S_{44} \end{pmatrix} \begin{pmatrix} I_i \\ Q_i \\ U_i \\ V_i \end{pmatrix} \quad (5.2)$$

Where:

$$I_s = E_{x, scat}^2 + E_{y, scat}^2 \quad (5.3)$$

$$\rightarrow I_s = S_{11}I_i + S_{12}Q_i + S_{13}U_i + S_{14}V_i \quad (5.4)$$

By computing the scattering at each point on the detectors surface we can compute the average scattering over the detector. From a experimental perspective the distance from the particle to the detectors must be considered. The near field scattering can be computed with relative ease using *mstm* as shown in

While *mstm* does provide the amplitude matrix it is not scaled to account for distance from the target to the detector. We amend this by simply scaling according to

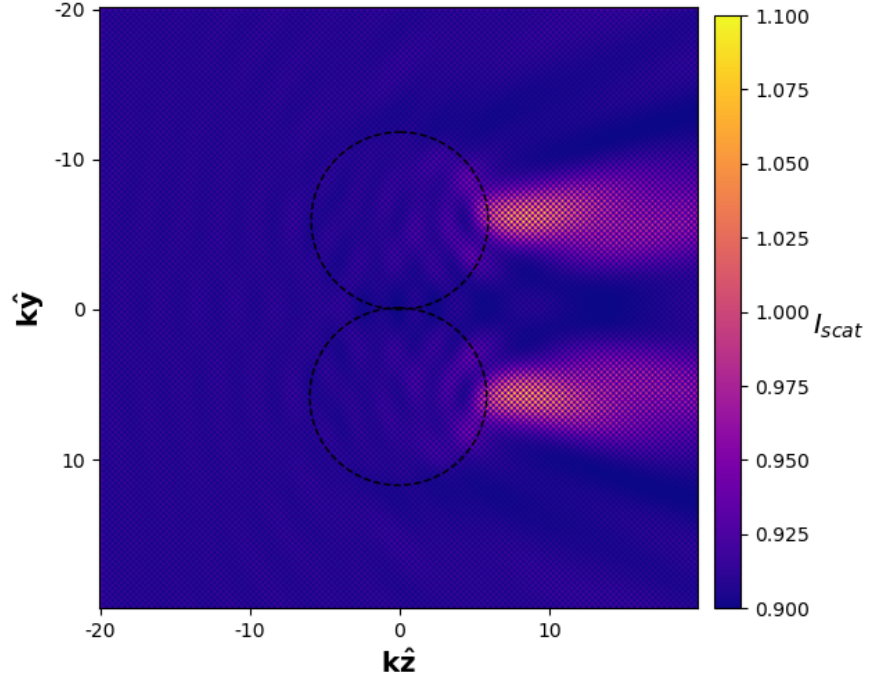


Figure 5.2: Intensity distribution (as defined by (5.3)) from a symmetric dimer when irradiated by the probe beam propagating in the $k\hat{z}$ direction (viewed in the z-y plane). Axis are given in dimensionless units of $k\hat{z}$ and $k\hat{y}$.

the inverse square law. As the detector is moved further from the target the intensity distribution across the entire detector will decrease substantially. Because of the fall off it is more computationally efficient to instead consider only the central pixel of the detector rather than across the entire surface. If we consider the difference between the average intensity and the intensity of the central point we can see that after not even 20μ away from the target particle the average intensity across the surface is within 0.1% of the central pixel.

Given the trapping beam's beam waist is approximately $0.54\mu m$, a optical fibre would need to be a minimum of $150\mu m$ from the trap centre in order to prevent noise from the trapping laser itself. At such a distance the variation in the signal is so small that it is easier to evaluate the intensity at the centre of the detector instead of across the entire surface. This is how the instantaneous orientation is predicted later on in

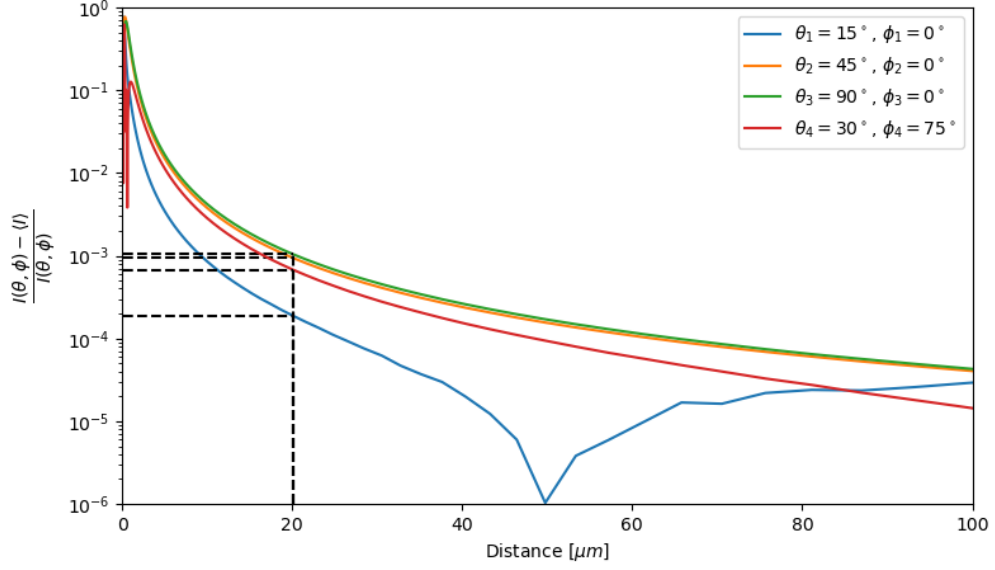


Figure 5.3: Normalised difference between the central pixel intensity $I(\theta, \phi)$ and the average pixel intensity over the surface of the optical fibre $\langle I \rangle$ as a function of distance. 4 different optical detectors were tested (spherical coordinates are given in the legend). While the choice of coordinates is arbitrary they all demonstrate the same exponential decay. Dashed lines indicate the difference after $20\mu m$ from the trap focus, in most practical cases getting an optical fibre any closer would disrupt the trap stability.

the chapter.

5.3 Interpretation of scattering data into orientation estimates

We now discuss the methodology for computing the instantaneous orientation of an optically trapped particle based on scattering detected by a finite grouping of optical fibres.

Consider a dimer in the optical trap (Fig. 5.4a), we can define at any point in time a unit vector \hat{s} pointing from the centre of the larger sphere to the centre of the smaller sphere. A plane wave probe beam incident, is incident on the dimer, generating a scattering pattern dependent on the dimer's orientation $I(\hat{s}, \theta, \phi)$ which is computed using *mstm* [4]. To represent the experimental set up consisting of a

set of optical fibres recording scattered light, we choose four sets of spherical angles $[(\theta_1, \phi_1), (\theta_2, \phi_2), (\theta_3, \phi_3), (\theta_4, \phi_4)]$ and record the calculated intensity at each angle $I(\hat{s}, \theta_k, \phi_k)$.

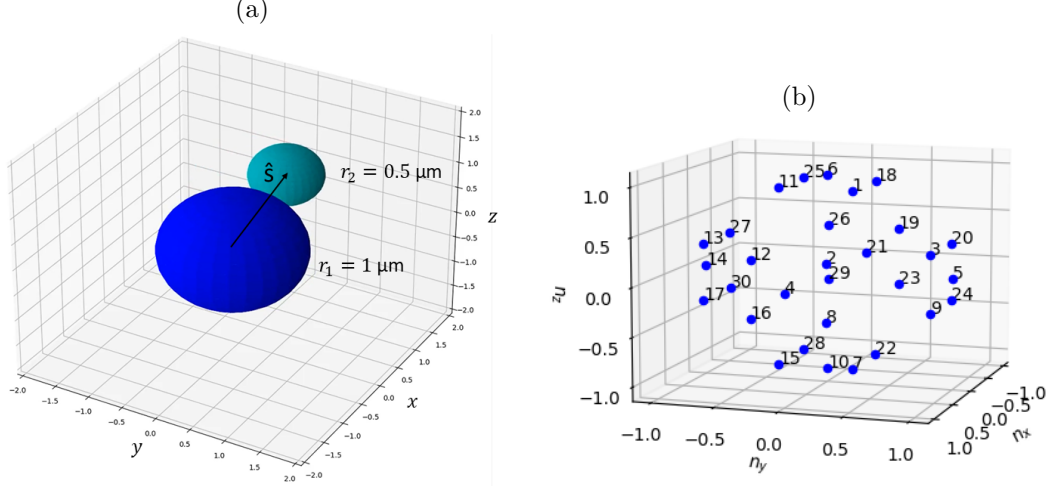


Figure 5.4: (a) Example dimer in orientation \hat{s} , (b) 30 Reference orientations represented by vectors pointing from $[0,0,0]$ to each point

Our goal is to determine the orientation of the trapped dimer based on the measured intensity $I(\hat{n}, \theta_k, \phi_k)$. Rather than aim an exact estimate of the dimer's orientation, for the purposes of interpretation of the scattering and optimisation of the measurement setup it is more convenient to discretize the possible orientation space into a number of possible reference orientations. We can then use each as 'classification categories' in a neural network methodology to map scattering data to orientation (see below for further discussion). Here we choose $n_{ref} = 30$ reference orientations \hat{n}_α evenly distributed on a unit sphere [6] (Figure 5.4b) leading to a maximum nearest neighbour spacing between two neighbouring reference orientations of 0.895 radians.

Using *mstm* we compute the raw intensities (see (5.3)) at each of the measurement angles that would be generated by a dimer in each reference orientation, $I_s(\hat{n}_\alpha, \theta_k)$. While the number and position of detection fibres is technically arbitrary there are several constraining factors that limit our ability to infer useful information from the trapped object, see Section 5.3.2 for a detailed breakdown of our choice of detection angles. In order for a neural network to properly weight each signal the raw intensities

are normalized according to:

$$y_k(\hat{\mathbf{n}}_\alpha) = \frac{I(\hat{\mathbf{n}}_\alpha, \theta_k) - \langle I(\hat{\mathbf{n}}, \theta_k) \rangle}{\langle I^2(\hat{\mathbf{n}}, \theta_k) \rangle - \langle I(\hat{\mathbf{n}}, \theta_k) \rangle^2} \quad (5.5)$$

where the denominator is simply the standard deviation across the set of values $I(\hat{\mathbf{n}}, \theta_k)$. Note that the collected scattering signals are not necessarily simply related to their associated reference orientations: as is well known from such examples of the inverse scattering problem. While it is trivial to compute the light scattering pattern for any given particle with any particular characteristic (i.e. size, shape, or orientation), inferring the light scattering from a unknown particle to determine said characteristic is incredibly difficult due to complex mapping between scattering and said characteristic. Even if the orientation space is divided evenly between reference orientations the subsequent signal space ends up being appearing mixed making simple comparisons of signals useless for inferring information on the particle.

Fig 5.5 shows two clusters of orientation vectors and their respective signals collected from 3 detectors - the points have been coloured based on their proximity to the centre of their respective cluster. While the orientation space appears tightly packed and ordered the signal space quickly spreads out in an asymmetric fashion. Furthermore as seen in Fig 5.5b the signal mapping can intersect itself which only further increases the complexity. While in some instances the mapping between one reference orientation and another is discrete, in other instances the mapping becomes far more complex to discern.

Nevertheless, at least where the uncertainty in signal measurements is low, we can predict the orientation from the scattering by utilising computational techniques such as neural networks. We thus utilised the Python machine learning program *scikit-learn* [5] to build a neural network for identifying the dimer's orientation from its light scattering signal. The network was trained by generating a database of random orientation vectors, calculating the corresponding light scattering signals, and then using the network to estimate the probability of a given signal coming from a dimer in a given reference orientation. The network's loss function was evaluated and

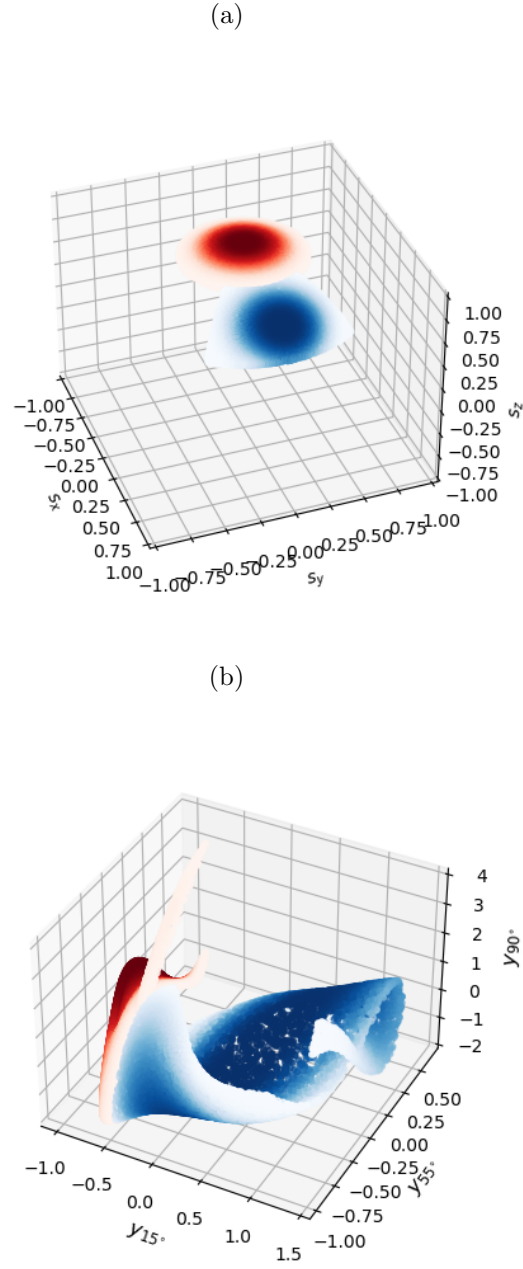


Figure 5.5: (a) Distribution of orientation vectors and (b) their respective scattering signals. Points are coloured according to their distance from the centre of each cluster (red points centred around $[0.00, 0.00, 1.00]$, blue points centred at $[0.71, 0.00, 0.71]$)

used to improve the estimation, the network being trained until the improvement in the loss function was less than 0.0001.

Importantly, the estimation provided by the neural network can be improved further by accounting for any prior information we know about the dimer, utilising Bayesian inference to update the neural network’s estimation:

$$p(\hat{\mathbf{n}}_\alpha | y_k(\hat{\mathbf{s}})) = \frac{p(y_k(\hat{\mathbf{s}}) | \hat{\mathbf{n}}_\alpha) p(\hat{\mathbf{n}}_\alpha)}{p(y_k(\hat{\mathbf{s}}))} \quad (5.6)$$

where $p(\hat{\mathbf{n}}_\alpha)$ and $p(y_k(\hat{\mathbf{s}}))$ are the prior estimates of the distributions of particle orientations and instantaneous signals, respectively. *Without* any prior evidence we must assume that the orientation prior of the dimer $p(\hat{\mathbf{n}}_\alpha)$ is uniform. However, inference about the dimer’s possible current orientation from knowledge of previous measurements can be used to inform our estimate of $p(\hat{\mathbf{n}}_\alpha)$. The latter prior $p(y_k(\hat{\mathbf{s}}))$ is the probability of measuring a signal (y_1, y_2, y_3) . This is given by taking the discrete integral over the collection of reference orientations:

$$p(y_k(\hat{\mathbf{s}})) = \sum_{\alpha=1}^{n_{\text{ref}}} p(y_1, y_2, y_3, y_4 | \hat{\mathbf{n}}_\alpha) p(\hat{\mathbf{n}}_\alpha) \quad (5.7)$$

From (5.6) we obtain the key result, a mass probability distribution denoting the probability that our dimer is in orientation $\hat{\mathbf{n}}_\alpha$ given a measured signal (y_1, y_2, y_3) , *i.e.* an estimated mapping from scattering measurement to orientation estimate.

5.3.1 Calculation of error

Using (5.6) we get a snapshot estimation of the instantaneous orientation of the trapped dimer based on a single measurement from a collection of detector signals. Of course in reality these detectors will be returning a discrete time series representative of the dimer’s trajectory within the optical trap.

Using the simulation code from [7] we can replicate this trajectory and furthermore use *mstmt* to calculate the far field intensity produced by said dimer. At each time step we measure the signal produced at each measurement angle and use our neural network to calculate $p(y_k(\hat{\mathbf{s}}) | \hat{\mathbf{n}}_\alpha, t)$.

Evaluating how well Eq. (5.6) performs in predicting $\hat{\mathbf{n}}$ is difficult because we have

discretised the orientation space meaning there will always be some degree of inaccuracy in our prediction. The Kullback-Liebler divergence method provides a measure of the relative entropy change between two probability distributions:

$$D_{KL}(P(t) \parallel Q(t)) = \sum P(t) \log_2 \left[\frac{P(t)}{Q(t)} \right] \quad (5.8)$$

Where $P(t)$ and $Q(t)$ are two probability distributions we are comparing, often it is common to use a base 2 log as this converts the entropy to base 2. By relative entropy we are talking about the useful information gained/lost by switching from $P(t)$ to $Q(t)$. In our case $Q(t)$ is simply the distribution given by Eq. (5.6) and $P(t)$ is an idealised distribution, one where the model is accurate with 100% certainty.

$$p_{best} = P(t) = \begin{cases} 1 & \text{when } \hat{\mathbf{n}}_\alpha = \hat{\mathbf{n}}_{best} \\ 0 & \text{when } \hat{\mathbf{n}}_\alpha \neq \hat{\mathbf{n}}_{best} \end{cases} \quad (5.9)$$

In reality the distribution from Eq. (5.6) will assign some non-zero probability to every reference orientation. Therefore the relative entropy for a single measurement is given as:

$$D_{KL}(p_{best} \parallel p(\hat{\mathbf{n}}_\alpha | y_k(\hat{\mathbf{s}}), t)) = \log_2 \left[\frac{1}{p(\hat{\mathbf{n}}_\alpha | y_k(\hat{\mathbf{s}}), t)} \right] \quad (5.10)$$

The relative entropy is a measure of how spread out our distribution is. With larger values of D_{KL} indicating that our prediction is spread out so the neural net is unsure about $\hat{\mathbf{n}}_{best}$. Whereas a low value of D_{KL} means that our model is more confident in $\hat{\mathbf{n}}_{best}$. The only drawback being that the relative entropy does nothing to indicate accuracy, only how closely our distribution matches our ideal result. This will be better exemplified later in 5.4.

5.3.2 Brownian Simulation

We use the Brownian OT package developed by Fung *et al* [7] to simulate the motion of an asymmetric dimer (Figure 5.4a) within an optical trap. We simulate the motion of a

Chapter 5. Detection and Characterisation of rotational spherical aggregate rotational dynamics

dimer trapped in a highly focused Gaussian beam by calculating the optical forces imparted by the laser, and the Brownian force due to the surrounding fluid. We simulated a polystyrene dimer ($n = 1.59$) in a suspension of water ($n_{med} = 1.33$). As discussed in chapter 4 dimers can be stably trapped in off-axis orientations. We simulate a dimer (of size ratio 2) that is trapped in this off-axis orientation by a $5mW$ laser, due to the meta-stability of the trap the dimer is only trapped for second before it escapes the trap. The dimer's position and orientation is shown below:

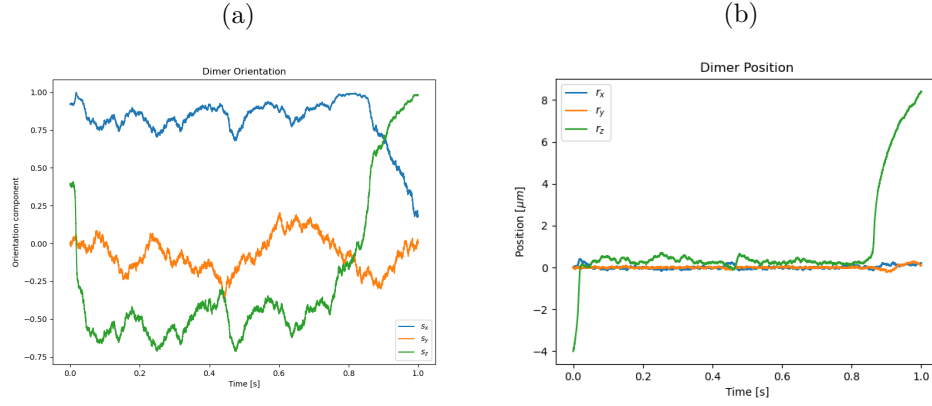


Figure 5.6: Simulation results of: (a) the dimer's orientation vector with time, (b) the dimer's $[x,y,z]$ position with time.

At the same we use *mstm* to replicate the intensity of light incident on the surfaces of detectors placed around the focus of the optical trap. The exact number of detectors was initially assumed to be arbitrary, in that it made no difference to our estimate whether we used 2 angles or 200. For practical purposes it seemed beneficial that we demonstrate our method works for a minimal number of detection angles, as geometric constraints come into play when trying to install a high number of detection fibres for any optical tweezer set up.

5.3.3 Choice on the number of detectors

When all of the detectors lie in the same plane the expected signal can appear identical despite the dimer being in completely different orientations. It should be noted that these pairs are reflected in one or more axis which suggests that these are due to the

arrangement of our detectors. More specifically, if the detectors are placed say in the x-y plane then only when the dimer is pointed nearly fully upright will the expected signal be entirely unique. This is not an issue with typical analytical static light scattering experiments because the signal being collected is averaged over a population of particles all in different orientations. Whereas in our set up we are concerned with the scattering of a single particle whose scattering is orientationally dependant.

To remedy this we raise the third detector out of the x-y plane; as such the expected signals from each reference orientation is unique, though with limited resolution. By adding a 4th detector we can differentiate signals more reliably, improving the neural networks performance. In line with our goal of making this method viable in a laboratory setting we decided not to increase the number of detectors further than 4.

5.4 Testing the Neural Network

We applied Eq. (5.6), taking the reference orientation with the highest probability as our estimate of the dimer's instantaneous orientation $\hat{\mathbf{n}}_{est}$. To visualise the model's performance we plotted the orientation components of our estimation $\hat{\mathbf{n}}_\alpha$ and the dimer's *actual* instantaneous orientation $\hat{\mathbf{s}}$ versus time. For comparison, we also plotted the orientation components of the closest reference orientation, $\hat{\mathbf{n}}_{best}$. Assuming a uniform prior of the reference orientations $p(\hat{\mathbf{n}}_\alpha)$ the neural network's predictions ($\hat{\mathbf{n}}_\alpha$ from Eq. (5.6)) are at times reasonable, but there are significant large and random jumps away from the correct result (Fig. 5.7).

One reason we observe such large jumps in the estimated orientation is simply because the neural network is assuming that the signals are unrelated from one another. We can observe this if we take the average relative entropy change across the entire trajectory:

$$\langle D_{KL} \rangle = \frac{1}{N} \sum_{i=1}^N \log_2 \left[\frac{1}{p(\hat{\mathbf{n}}_\alpha \parallel y_k(\hat{\mathbf{s}}, t_i))} \right] \quad (5.11)$$

Where we get an average entropy change of ≈ 0.604 , in base 2 this means that on

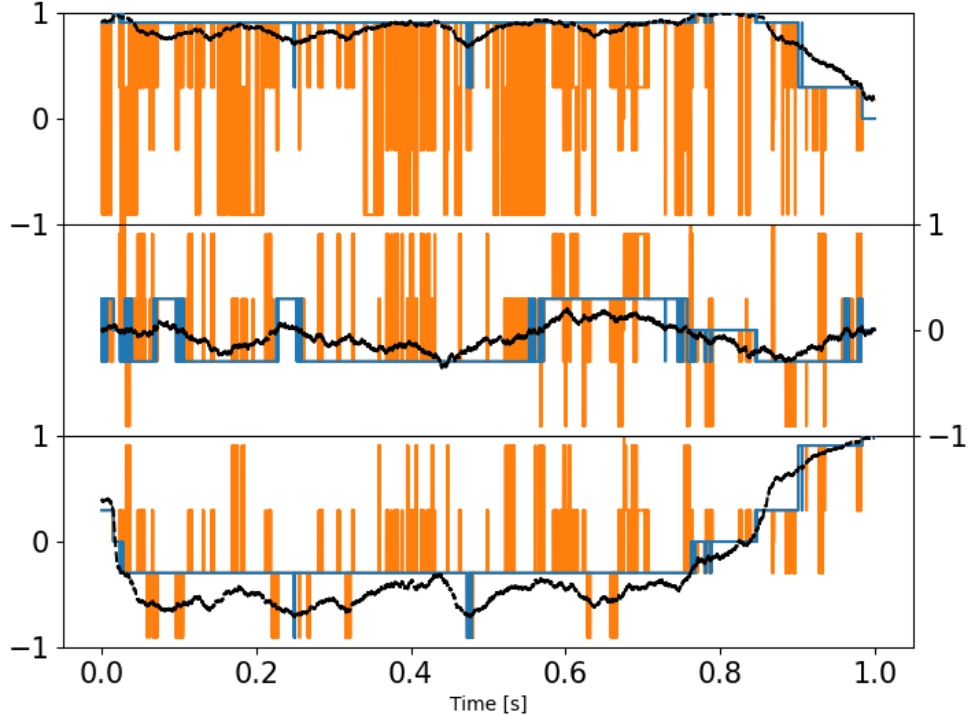


Figure 5.7: Model’s estimation of dimer orientation over the simulation time, assuming uniform prior $p(\hat{\mathbf{n}}_\alpha)$, broken up into x, y, and z components for clarity. Blue line denotes the best result we can achieve (the reference orientation $\hat{\mathbf{n}}_{best}$ that is closest to the actual orientation), orange line denotes the result provided by eq 5.6: where the blue line is not visible, the model’s prediction agrees with $\hat{\mathbf{n}}_{best}$. Dotted black line is the instantaneous orientation $\hat{\mathbf{s}}$.

average the model has narrowed down its options from 1 in 30 to 1 in 1.52. This is not reflected though in fig. 5.7 which indicates that while the model is highly confident in its results it is not at all accurate. As demonstrated by fig 5.5 the orientation and signal spaces are uncorrelated with one another which results in the neural network to assign orientations incorrectly. Combining this fact with use of a uniform prior ($p(\hat{\mathbf{n}}_\alpha)$), there is no constraint on how much estimated orientation can change from time-step to time-step.

To improve the estimation we can therefore use knowledge of the physical limitations of the object in the trap and its dynamics. Imposing a more physically grounded prior,

accounting in this case for the fact that the rotational motion of the dimer is limited by the rotational trap stiffness (κ_r). Here the prior of the reference orientations $p(\hat{\mathbf{n}}_\alpha)$ was redefined at each time step as a Boltzmann distribution of the physical distance between the previous estimate $\hat{\mathbf{n}}_{est}(t - \Delta t)$ and each reference orientation $\hat{\mathbf{n}}_\alpha$. Put simply, we are reweighing our estimation based on the size of rotation, with smaller movements being favoured over large movements:

$$p(\hat{\mathbf{n}}_\alpha) = \frac{e^{\hat{\mathbf{n}}_\alpha \cdot \hat{\mathbf{n}}_{est}(t - \Delta t)}}{\sum_{\alpha=1}^{n_{ref}} e^{\hat{\mathbf{n}}_\alpha \cdot \hat{\mathbf{n}}_{est}(t - \Delta t)}} \quad (5.12)$$

As shown in Figure 5.8 implementation of Eq (5.12) helps significantly reduce the large random excursions of estimated orientation away from the 'best' result. However at the same time result is still subpar.

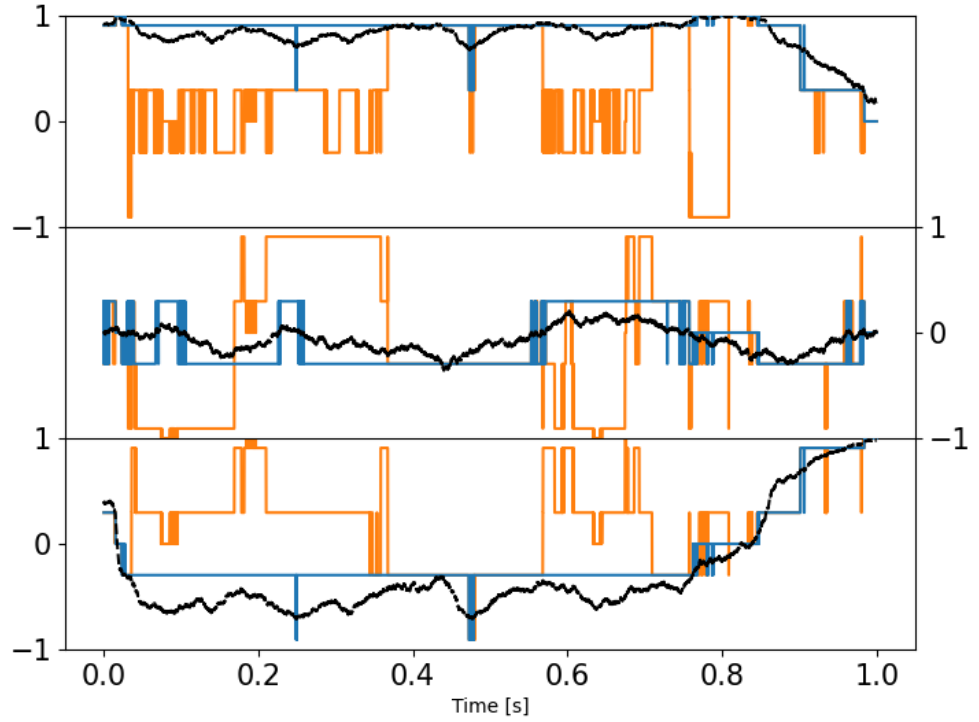


Figure 5.8: Estimation of dimer orientation with $p(\hat{\mathbf{n}}_\alpha)$ defined by Eq (5.12). Blue line denotes the best result we can achieve, orange line denotes the result provided by eq 5.6. Dotted black line is the instantaneous orientation $\hat{\mathbf{s}}$ (see Section ??).

Once again using Eq. (5.11) we now get a result of ≈ 0.204 or a 1 in 1.2 result. This is only a slight improvement in terms of confidence but has drastically reduced the variation in our models predictions. There are other improvements that can be made, which additionally also help with potential sources of error in our set up.

5.5 Accounting for sources of error in light scattering measurements

When it comes to analysing light scattering from any size particle, error analysis becomes a significant factor. Typically this can be accounted for by averaging over long periods of time to get an assessment of the steady state conditions of the target particle. However in our case where we wish to know the instantaneous orientation, we instead have to rely on our understanding of how uncertainty can effect our model's performance. We identified two areas which are likely sources of error in our estimation: firstly, an incorrect modelling of the target particle, and secondly, signal noise arising from experimental factors. We highlight how we address these areas below.

5.5.1 Impact of incorrect dimer sizing

One of the main limitations of our model is that we assume that the dimer being modelled in *mstm* is accurate to the dimer being trapped in the optical tweezer. Sizing molecules accurately is a significant challenge for single particle analysis so there is bound to be some uncertainty with the measurements. We ran our model 3 times with the neural net being trained on a dimer of size ratio 1 : 1.95, 1 : 2.00 and 1 : 2.05.

As can be seen from Fig 5.9 even the slightest change in size ratio makes a very significant difference to the performance of our model. This amounts to just over 100 *nm* in the dimer's overall size, yet results in our model being correct from over 90 % of the time to now as low as 30 %. This highlights the importance of correctly sizing trapped entities before performing any in depth analysis of the scattering pattern, as even the slightest deviation can have a serious impact. We addressed this by increasing the number of available reference orientations from 30 to 126 (following the same procedure

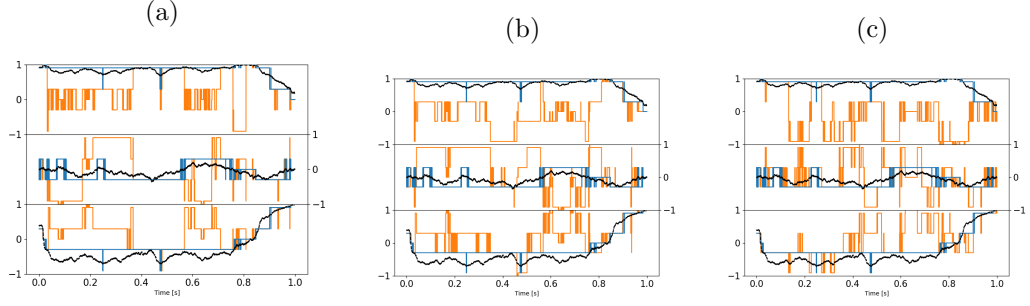


Figure 5.9: Model estimates of orientation when neural net has been trained on dimer of size ratio: (a) 1:2 [$\langle D_{KL} \rangle = 0.519$], (b) 1:2.05 [$\langle D_{KL} \rangle = 3.706$], (c) 1:1.95 [$\langle D_{KL} \rangle = 3.705$] ($n_{refs} = 30$)

as given by [6] to evenly space out the coordinates) and increasing the weighting factor in Eq 5.12. While this didn't have a significant improvement on the overall accuracy of the model, in the worst case having a slight increase from 30.5 % to 40.3 %, it did help to significantly reduce the magnitude between our model's estimations and the dimer's motion as seen below in Fig 5.10.

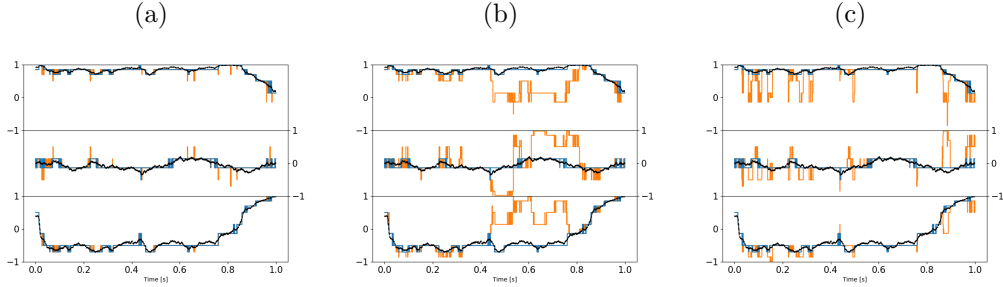


Figure 5.10: Model estimates of orientation when neural net has been trained on dimer of size ratio: (a) 1:2 [$\langle D_{KL} \rangle = 0.593$], (b) 1:2.05 [$\langle D_{KL} \rangle = 5.659$], (c) 1:1.95 [$\langle D_{KL} \rangle = 3.279$], ($n_{refs} = 126$)

Notably the increasing the number of reference orientations had a greater effect when our neural network was trained on a 1:1.95 dimer than a 1:2.05 dimer. This suggests that overshooting our size estimate will be less detrimental to our estimation. Notably if the our sizing is off the neural network does not predict a smooth motion within the trap; instead predicting that the dimer is jumping back and forth between different orientations. This suggest that we can narrow down our estimate of the

particle's size by assessing how the dimer is reorienting within the trap, as we should expect a smooth continuous prediction. Since we are working with a spherical dimer it also stands to reason that techniques such as image analysis could be used in part to address this, so long as the trapped entity is sufficiently illuminated.

5.5.2 Impact of measurement noise on model predictions

So far a key assumption of the neural network implementation is that the detected scattering signal has no uncertainty associated with it. In reality of course scattering signals will always have some non-zero measurement noise. This can be attributed to a variety of factors, from a measurement bias in the detector, to the Brownian motion of the dimer itself. To explore the impact of measurement uncertainty on orientation estimation model performance we introduce a Gaussian noise to the measured signal:

$$I(\hat{\mathbf{s}}) = I(\mathbf{\hat{s}}) \pm \epsilon I(\mathbf{\hat{s}}) \quad (5.13)$$

where ϵ is the percentage error associated with the scattering signal. Figure 5.11 shows the performance of the model at a range of ϵ using in-plane detector angles 15° , 55° , 90° and out-of-plane detector at 75° , with β set to 1:

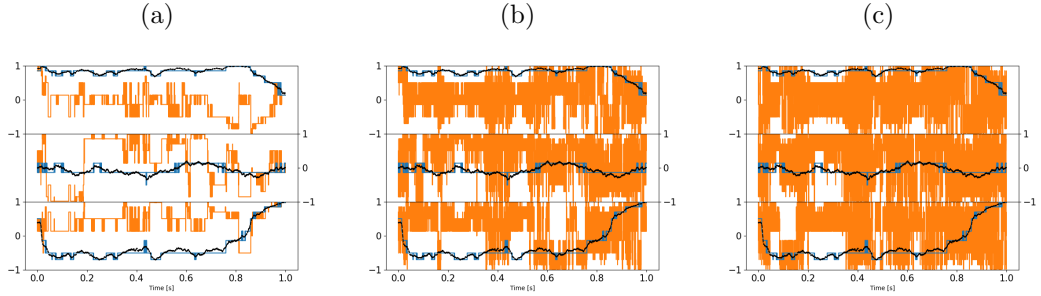


Figure 5.11: Model prediction for signal error of (a) 1% [$\langle D_{KL} \rangle = 0.962$], (b) 15% [$\langle D_{KL} \rangle = 13.654$], and (c) 25% [$\langle D_{KL} \rangle = 13.017$].

As can be seen from Figure 5.11, the inclusion of signal noise quickly leads to a decrease in the model's performance. So much so that beyond 15% the model is actually worse than just randomly guessing. This is due to an inherent feature of the inverse scattering problem: two distinct regions in orientation space can become heavily

intertwined and thus no longer well separated when mapped to intensity space (even though the mapping remains continuous): so even small uncertainties in the scattering data can lead to large 'mistakes' in the choice of orientation by the neural network. (Indeed if this was not the case the inverse scattering problem would be quite simple.)

To reduce the effects of the signal noise we took the time average of the expected signal over 0.001s and then had our neural network estimate the orientation based on the average signal.

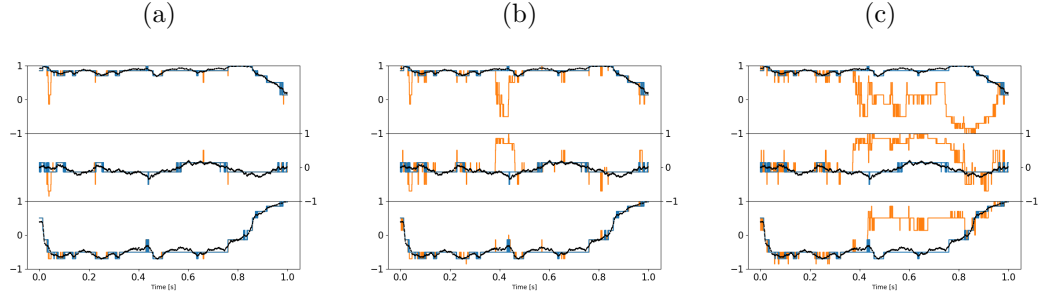


Figure 5.12: Model prediction for signal error of (a) 1% [$\langle D_{KL} \rangle = 1.447$], (b) 15% [$\langle D_{KL} \rangle = 4.670$], and (c) 25% [$\langle D_{KL} \rangle = 7.911$], time averaged over 1 ms

This resulted in a reduction in the overall signal noise and provided a higher degree of accuracy for our model. There appears to be no clear correlation between the length over which we time average and the performance of our model. Time averaging over every 0.05s resulted in a drastically worse performance; this is due to the fact that over longer time periods there is greater uncertainty regarding how the dimer's orientation has changed, thus tracking the instantaneous orientation becomes harder for the neural network. Fortunately, time averaging even over 1 ms seems to provide a satisfactory estimation of the dimer's angular dynamics within the optical trap.

Overall it's clear that estimation of the dimer's orientation is a problem that can be endlessly tuned to optimise the result. Here we simplify the problem somewhat by employing a relatively small finite number of 'reference orientations' to map between scattering and dimer orientation: the precision of estimation could be improved by utilising a greater number of reference orientations, although there remains a balance between the realisable precision of orientation estimate and the noise level of the scattering mea-

surement. Another avenue to further explore would be using the method to optimise the choice of detection angles, essentially to find the region in the mapping between measured scattering and orientation that offers the best degree of confidence through optimal separation of scattering signals for distinct orientations. For sequences of data such as dynamic measurements, a further potential enhancement would be to consider more complex correlations based on prior expectations of the dynamics. The Debye equation for Here already we improve the method using a non-uniform prior based on only the immediately previous measurement in time (see Section 2.1): considering a non-uniform grouping of reference orientations might result in a better estimation, if we have information regarding the dimer’s preferred axis of rotation.

5.6 Conclusion

We have developed a method for measuring the dynamics of an optically-trapped colloidal objects based purely on measurements of the object’s light scattering at a small number of detection angles. We demonstrate the method using the orientation of an asymmetric dimer as the dynamic variable and object of interest respectively, but in principle the model can be applied to any characteristic that impacts the light scattering pattern produced by a trapped entity such as size and shape. The MSTM package is a flexible tool for calculating the light scattering of complex objects using a representation of the object as a set of micro-particles, enabling training of a neural network to enable categorisation of the mapping between scattering and trapped object characteristics. By taking account of the physically realistic behaviour of the trapped object and the characteristics of the trap (which impact the dynamics of the object), the Bayesian inference method can be refined to provide a reliable estimation of object characteristics of interest, even in the presence of measurement noise. Fundamentally, the inverse scattering problem is difficult to solve, since the mapping between object characteristics and scattering can be highly complex. We determined the minimum number of detectors required for a reliable estimation in the presence of measurement noise; furthermore, we demonstrated that the arrangement of these detectors is critical

Chapter 5. Detection and Characterisation of rotational spherical aggregate rotational dynamics

for a reliable estimation of an objects orientation. However, Bayesian inference based on neural network estimation of the mapping provides a powerful method for practical applications, extending the use of optical trapping beyond measuring microscopic force response toward detailed structural and dynamic information about complex trapped entities.

Conventional calibration methods will not be adequate however, while angular motion can be detected using complicated set ups [1], this can only provide an estimate of the magnitude of a particle's angular motion. This is perfectly fine in cases where the rotational motion is stochastic and intuitively predictable (i.e. a dimer in a vertical orientation undergoing stochastic Brownian motion), but in the case the the motion is instead periodic characterising it requires instantaneous measurements of the particle's motion.

Bibliography

- [1] Jaehoon Bang, T. Seberson, Peng Ju, et al. “Five-dimensional cooling and non-linear dynamics of an optically levitated nanodumbbell”. In: *Physical Review Research* 2.4 (Oct. 2020), p. 043054. ISSN: 2643-1564. DOI: 10.1103/physrevresearch.2.043054.
- [2] R. Bar-Ziv, A. Meller, T. Tlustý, et al. “Localized Dynamic Light Scattering: Probing Single Particle Dynamics at the Nanoscale”. In: *Physical Review Letters* 78.1 (Jan. 1997), pp. 154–157. ISSN: 1079-7114. DOI: 10.1103/physrevlett.78.154.
- [3] Kirstine Berg-Sørensen and Henrik Flyvbjerg. “Power spectrum analysis for optical tweezers”. In: 75 (2004), pp. 594–612. ISSN: 0034-6748. DOI: 10.1063/1.1645654.
- [4] Daniel W. Mackowski Michael I. Mishchenko Larry D. Travis. “T-matrix computations of light scattering by nonspherical particles: A review”. In: *Light scattering by Non-Spherical Particles* 55 (1996), pp. 535–575.
- [5] F. Pedregosa, G. Varoquaux, A. Gramfort, et al. “Scikit-learn: Machine Learning in Python”. In: *Journal of Machine Learning Research* 12 (2011), pp. 2825–2830.
- [6] Guillem Colomer Reythor. “Numerical methods for radiative heattransfer”. Doctoral Thesis. Universitat Politècnica de Catalunya, 2006.
- [7] Wyatt Vigilante, Oscar Lopez, and Jerome Fung. “Brownian dynamics simulations of sphere clusters in optical tweezers”. In: *Optics Express* 28.24 (Nov. 2020), p. 36131. ISSN: 1094-4087. DOI: 10.1364/oe.409078.